Post-print version of:

Title: **Fretting fatigue of aluminum alloy in contact with steel in oil drill pipe connections, modeling to interpret test results**

Authors: **C. Santus**

Fretting fatigue of aluminum alloy in contact with steel in oil drill pipe connections, modeling to interpret test results

C. Santus *

Dipartimento di Ingegneria Meccanica, Nucleare e della Produzione.
Università di Pisa. Via Diotisalvi n°2 - 56126 - Pisa. Italy.

Abstract

In many drilling sites for oil production, the use of high strength aluminum alloy for the drill-string can be preferable than steel, due to its better strength over weight ratio, lower stiffness and higher corrosion resistance. This leads to the need of aluminum to steel pipe connections, which can be critical in terms of fatigue. The design of this connection is prone to Fretting Fatigue similar to the shrink-fitted assembly of a shaft in a housing. Full scale tests are reported in the present paper, showing a reduction of the fatigue strength, due to fretting, by a factor around 2.7, in comparison to aluminum alloy fatigue strength.
The Theory of the Critical Distance along with the Modified Whöhler Curve Method can give good results in interpreting full scale tests, however a slip related parameter, to better characterize the fretting condition, is introduced. Then a two parameters (stress–slip) map is proposed, which can offer a powerful tool to evaluate modifications of the design, to improve fretting fatigue performance.

Key words: Fretting Fatigue. Critical Distance. Full Scale Tests. Aluminum Drill Pipe to Steel Tool Joint Connection.

—————
* Corresponding author: Ciro SANTUS
E-mail address: `ciro.santus@ing.unipi.it`
Phone: +39 320 4212184
Fax: +39 050 836665

Notation

σ_0	[MPa]	Bending nominal stress amplitude acting on connections.
σ	[MPa]	Axial stress amplitude acting on small scale specimens.
R	[–]	Monoaxial load ratio.
N_f	[N]	Number of fatigue cycles up to final failure.
N_e	[–]	Endurance fatigue limit.
E_1	[MPa]	Steel Young modulus.
E_2	[MPa]	Aluminum alloy Young modulus.
ν_1	[–]	Steel Poisson ratio.
ν_2	[–]	Aluminum alloy Poisson ratio.
f	[–]	Coefficient of friction.
α	[–]	First elastic Dundurs' parameters.
β	[–]	Second elastic Dundurs' parameters.
K_I^*	[MPa m$^{-1/2}$]	Contact pressure generalized stress intensity factor.
K_{II}^*	[MPa m$^{1/2}$]	Shear traction, generalized stress intensity factor.
c	[mm]	Cyclic slip length.
P	[N m^{-1}]	Normal load, per unit length, acting on the indenter.
Q	[N m^{-1}]	Shear load, per unit length, acting on the indenter.
σ_b	[MPa]	Bulk stress, acting below the contact interface.
$\Delta\sigma_b$	[MPa]	Bulk stress range.
r'	[mm]	Distance from the sharp edge (complete contact).
r	[mm]	Distance from edge of contact (incomplete contact).
$p(r)$	[MPa]	Pressure distribution.
$q(r)$	[MPa]	Shear traction distribution.
ΔK_{th}	[MPa m$^{1/2}$]	Stress intensity factor threshold range.
σ_∞	[MPa]	Axial stress fatigue limit amplitude.
$\Delta\sigma_\infty$	[MPa]	Axial stress fatigue limit range.
τ_∞	[MPa]	Torsion stress fatigue limit amplitude.
L	[mm]	Material critical distance.
θ, ϕ	[rad]	Angles defining the generic plane orientation.
θ^*, ϕ^*	[rad]	Angles defining the critical plane orientation.

τ_a	[MPa]	Shear stress amplitude acting on the critical plane.
$\sigma_{n,max}$	[MPa]	Maximum normal stress acting on the critical plane.
ρ	[–]	Multiaxial load ratio, $\rho = \sigma_{n,max}/\tau_a$.
ρ_1	[–]	Multiaxial load ratio of small scale specimen series 1.
ρ_2	[–]	Multiaxial load ratio of small scale specimen series 2.
κ	[–]	Exponent defining the *S-N* curve slope.
κ_1	[–]	*S-N* curve slope of small scale specimen series 1.
κ_2	[–]	*S-N* curve slope of small scale specimen series 2.
$\sigma_{\infty,1}$	[MPa]	Axial stress fatigue limit amplitude of small scale specimen series 1.
$\sigma_{\infty,2}$	[MPa]	Axial stress fatigue limit amplitude of small scale specimen series 2.
τ_a^{eq}	[MPa]	Equivalent torsion stress, according to MWCM.
S_Y	[MPa]	Static Yield limit.
S_{UTS}	[MPa]	Ultimate Tensile Stress.
s	[μm]	Slip along the contact coordinate *r*, during time.
s_0	[μm]	Slip at the edge of contact $r = 0$, during time.
s_a	[μm]	Slip amplitude, at the edge of contact $r = 0$.
p_{max}	[MPa]	Maximum contact pressure along the contact, during time.
FE		Finite Element.
FF		Fretting Fatigue.
TCD		Theory of Critical Distance.
PM		Point Method, of the TCD.
MWCM		Modified Whöhler Curve Method.
ADP		Aluminum Drill-Pipe (technical term related to oil drilling).
STJ		Steel Tool-Joint (technical term related to oil drilling).

1   Introduction

The *drill string* is a long (up to several kilometers) flexible (around 100-200 mm in diametrical cross section) tubular structure which drives the drill bit to produce the well for oil production [1]. The drill string is composed by hundreds of segments (*drill pipes*) joined by threaded connections (*tool joints*). Failures, usually located at the connections, are due to material fatigue, aggravated by corrosive environment [2,3] primarily related to hydrogen sulfide, improper equipment handling, excessive rotational speeds or weight on bit. Failure of the drill-string is one of the most frequent and costly problem during oil drilling [4].
Usually material to produce drill pipes, an their connections, is quenched and tempered (at high temperature) Chromium-Molybdenum steel. However in some drilling sites it turns out to be cost effective the use of high strength aluminum alloy drill pipes [5], connected by steel tool joints.
The most important advantages of using aluminum alloy instead of steel are:

- higher strength over weight ratio, indeed static loads are just due to the weight of the drill string itself;
- lower stiffness, since very often wells are deviated then the string can accomplish bends more easily;
- higher corrosion resistance.

The main disadvantage is the high rate of wear against rocks during drilling.
According to just showed advantages and disadvantages, Titanium alloys could offer even a better solution [5], however the cost of the material can drive the choice toward the use of aluminum alloys.
During drilling operations, connections need to be open and closed very often [1], then the connection need to remain manufactured in steel otherwise the thread will experience very quick damage.
To satisfy this requirement the aluminum drill pipe (ADP) is connected to the steel tool joint (STJ), and the tool joints (*Pin* and *Box*) are connected after, as shown in Fig. 1, according to standard [6].
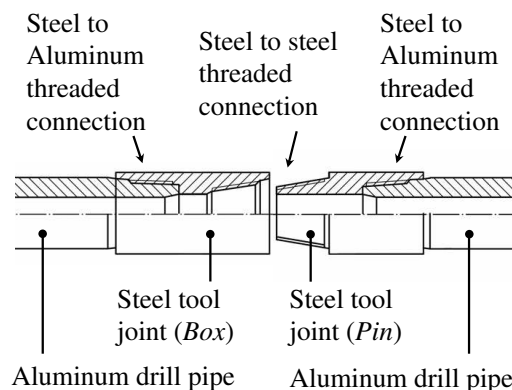

Fig. 1. Connection between aluminum drill pipe and steel tool joint.

In this way the connection steel to steel can be frequently opened and closed during

drilling, while the aluminum to steel threaded connections can remain closed during its whole service life.

The material considered in the present paper is a high strength aluminum alloy, its composition is reported in standard [6], and it is very similar to AA 7014 (Zn: 5.5–6.0, Mg: 2.4–3.0) [7]. Well known aluminum alloy AA 7075 has almost same composition in terms of Zn and Mg, but AA 7014 has lower content of Cu. The static yield limit is $S_Y = 490$ MPa and the ultimate tensile stress is $S_{UTS} = 540$ MPa.

Since the well, produced by drilling, is very often not straight, the drill string need to rotate inside a bend. Its high flexibility allows the string for accomplish the path easily, but the connection experiences rotating bending fatigue which is usually the primary failure mode. Therefore fatigue strength of the connection is a strategic piece of information for drilling companies.

Considering the connection fatigue failures more closely, it is remarkable that the steel never fails, while only aluminum does. The fatigue failure site is in contact with the edge of the thread free portion of the steel connection, which generates Fretting Fatigue (FF) on the aluminum cylindrical surface, Fig. 2.
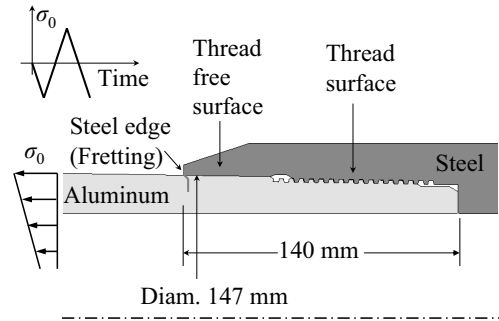

Fig. 2. Fretting fatigue site, where the crack nucleates.

Full scale fatigue tests were performed through a dedicated test rig, designed and produced, at the Mechanical department of the University of Pisa, and the first set of results are here published. The design of the test rig is proposed in Ref. [8], but it is not in the scope of the present paper.

Fatigue failures obtained were in agreement to Fig. 2. It is remarkable that the thread which is an evident stress concentration site does not generate fatigue failure, since the thread free portion of the connection shields the cyclic stress at the last engaged thread root. If the construction had not the thread free surface, then the last engaged thread root would be exposed to fatigue quite strongly and the connection would be much weaker than the current design is.

2 Experimental evidence of fretting fatigue on full scale tests

In Fig. 3 full scale tests of aforementioned aluminum to steel connections, are reported. The loading condition is rotating bending without mean axial loading ($R = -1$), and the bending stress σ_0, just away from the connection, is here considered as the nominal stress.

Small scale testing on plain specimens, performed at fully reversed axial loading ($R = -1$), are also reported in Fig. 3, to show a comparison with the material fatigue strength.
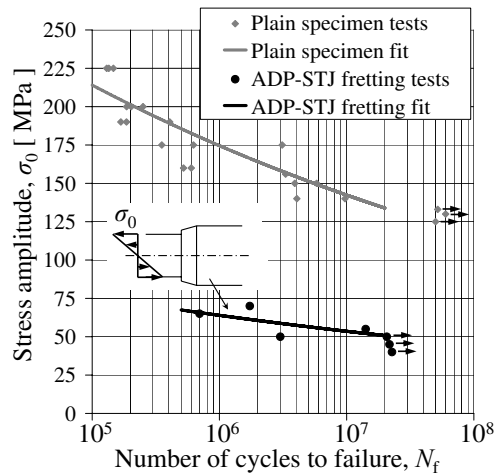

Fig. 3. Full scale test results, comparison to the material fatigue strength, obtained with small scale plain specimens.

Four tests produced FF failure while three run-out were obtained considering the endurance limit at $N_e = 20\,10^6$ cycles.

By comparing the two lines a sort of *fatigue factor* can be defined as the ratio between the fatigue limit of the plain specimen over the fatigue limit of the connection. This stress ratio is 2.7 at endurance limit $N_e = 20\,10^6$.

An important issue, deeply investigated in the present paper, is that the two sides of the connection were loaded with the same bending stress, but failures were found at one side only. The only difference in design, between the two sides, is the chamfer angle, Fig. 4.
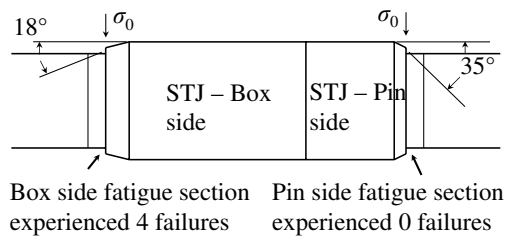

Fig. 4. Different fatigue performances at the two sides of the connection.

This comparison between the two sides offers a valid insight to investigate, then it is carefully taken into consideration in the paper.

In Fig. 5 evidence of FF nucleation is shown. Indeed the position where the fatigue crack nucleates is just below the small fillet (radius = 2 mm) of the steel edge, Fig. 5 (a). Moreover the crack path resembles the common fretting crack extending below the fretting interface, up to a certain distance and then following the crack mode I propagation [9]. Finally in Fig. 5 (b) the fretted strip, around the cylindrical aluminum surface, is shown.

It is worth noting that the large marks below the fretted strip, Fig. 5 (b), were produced after the structure lost its integrity (very large crack, close to final failure)
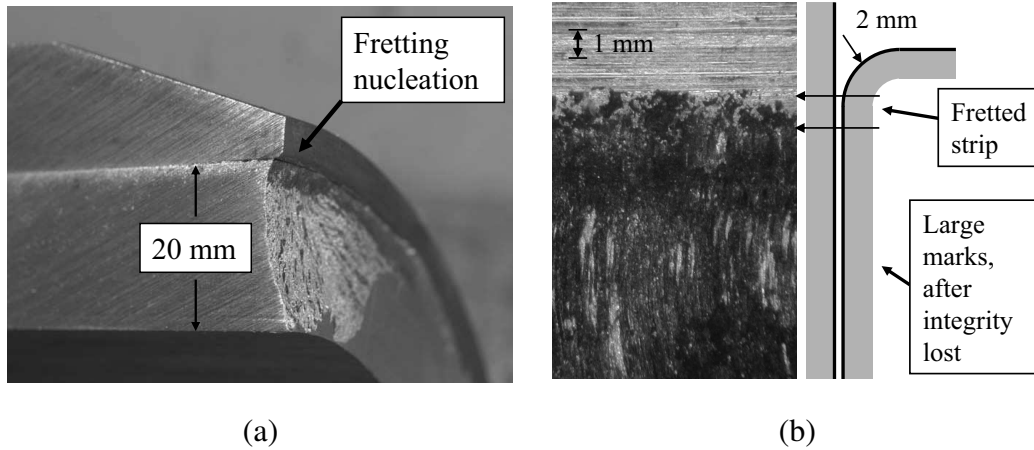
6

Fig. 5. (a) Fretting nucleation at the flat and rounded edge. (b) Evidence of the fretted strip, near to the fretting nucleation position.

then gross slip acted on the surface.

This common fretting configuration is similar to the shrink-fitted assembly of a shaft in a housing (discussed in the Waterhouse text book [10]) loaded by rotating (or alternating) bending, and the fretting site is the typical flat and rounded edge contact.

3 Stresses distribution at the flat and rounded edge

As previously introduced the fatigue crack nucleation site was observed on the aluminum side at the flat and rounded edge contact. Local stresses at this location are caused by:

- radial interference, producing contact pressure between aluminum and steel surfaces;
- external bending loading, generating:
  · shear traction between the two surfaces in contact;
  · contact pressure transfer from the tensile side to the compression side, due to deflection;
  · cyclic bulk stress $\Delta\sigma_b$ acting below the contact, in phase with the shear traction.

It is remarkable that without radial interference, bending would produce contact loss at the tensile side. While imposing a certain level of radial interference there is no contact loss, however pressure distribution experiences cycling. Moreover, the higher the radial interference, the smaller the slip length and the slip amplitude, but the higher the shear traction. Regardless these issues, at the design stage, the radial interference is usually prescribed high enough to obtain connection sealing and strength against torsion.

Contact pressure distribution and shear traction distribution, during bending, are qualitatively depicted in Fig. 6.
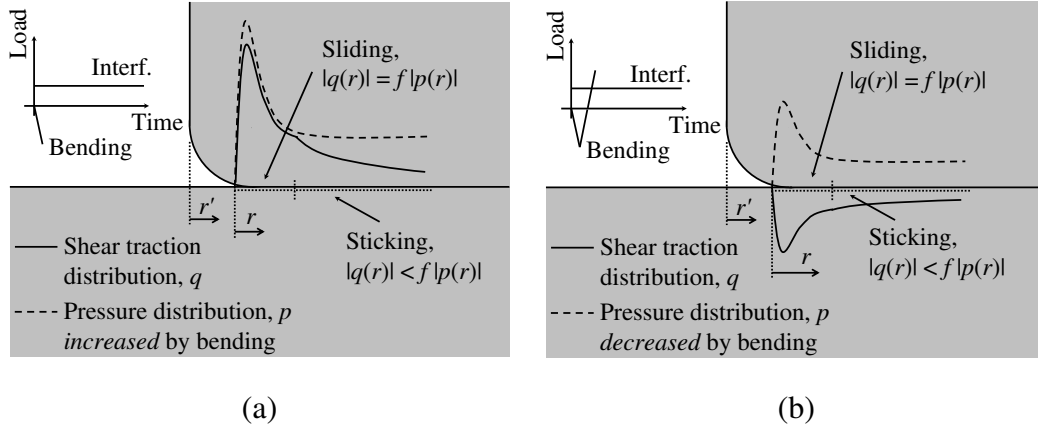
Fig. 6. Local stress generated at the flat and rounded edge, by loading the component applying bending after imposing interference: (a) bending increasing contact pressure, (b) bending decreasing contact pressure.

Considering the square ended steel ($E_1 = 205\,000$ MPa, $v_1 = 0.3$) in contact with aluminum ($E_2 = 73\,000$ MPa, $v_2 = 0.3$) half plane, the contact pressure distribution would follow the asymptote $p(r') \propto r'^{-0.348}$ near the sharp corner, if frictionless contact was assumed (Dundurs' parameters $\alpha = 0.4748$) [11,12], where r' is the local coordinate starting from the *sharp* edge (Fig. 6 considering no fillet).

The celebrated work of Giannakopoulos et al. [13] correctly indicates that the asymptote $p(r') \propto r'^{-0.5} = 1/\sqrt{r'}$ (suggesting the crack analogue) can be obtained only if the punch is rigid and the half space is incompressible, or if the punch is rigid and the contact is frictionless. In frictionless condition, considering the actual stiffness of the punch (steel is stiffer than aluminum, but not *infinitely* rigid) the order of the singularity is $r'^{-0.348}$, as mentioned before, lower than $1/\sqrt{r'}$ (elastic similar materials configuration shows even lower order of singularity: $r'^{-0.226}$). Moreover in friction condition, the pressure distribution is coupled with the shear traction, either due to dissimilarity of the materials (steel in contact with aluminum) and for not having both half plane geometry [14]. In this condition ($\alpha = 0.4748$, $\beta = 0.1357$) from maps proposed in Ref. [11], it is possible to deduce that for high coefficients friction (f near 1.0 or higher) the pressure distribution is bounded when the contact is *trailing* (tensile phase of bending, in the present configuration), i.e. the pressure distribution is not singular. On the contrary during the opposite phase the order of singularity gets worse, for example for a large value of the coefficient of friction, $f = 1.0$, it reaches the singularity of $r'^{-0.460}$.

Considering the presence of the macroscopic fillet, the contact is incomplete due to the fillet (flat and rounded edge), then the pressure distribution falls to zero where the contact ends. Near the edge of contact the pressure distribution features the competition of two asymptotes [15,16]:

- the singular solution asymptote, termed *outer* asymptote, that would be found according to complete contact condition (square ended edge at any scale level, instead of flat and rounded edge);
- the square root bounded asymptote (according to the Hertz solution) termed *inner* asymptote.

8

The outer asymptote solution is no longer valid very near to the fillet (where the inner asymptote solution dominates) and it is also no valid far from the edge where uniform pressure distribution can be found. The presence of a macroscopic fillet reduces the interest about the outer asymptote. Indeed the process volume involved in the fretting crack nucleation has usually a size comparable to that of the volume whose stress distribution is influenced by the inner asymptote. This is particularly true if the *averaging length parameter*, used in Ref. [17], or the *critical distance* in Ref. [18] (more details are given later), that give a measure of the size of the process volume, are comparable or smaller than the fillet radius. Even if this is true for the present configuration, it is not generally valid. In the case of very little fillet radius (for example nominally sharp) in comparison to material critical distance, the stress solutions would be dominated by the outer asymptote.

Neglecting the dissimilar material effect (that couples contact pressure to shear traction, induced by friction) the pressure distribution falls as the square root of the distance from the edge of contact, as the Hertz plane contact solution (inner asymptote). However the use of FE does not require to neglect the coupling effect, which is automatically reproduced by the model. Since the contact pressure is bounded, the shear traction is limited by the coefficient of friction f approaching toward the edge of contact, and then a slip region need to exist before a stick region [19]. Due to large bulk stress cycling, in phase with the shear traction, the slip length is extending in the flat portion of the contact [20]. At the curvature discontinuity point, where the fillet is merged to the flat portion (referred as the *hot spot*) the pressure distribution features local infinity derivative, falling from the round portion of contact toward the flat portion of contact [21].

As already mentioned, contact pressure distribution is intensified in one direction of bending and reduced at the opposite direction, as compared to distribution produced by radial interference alone. Shear traction distribution follows this trend as well since because in the slip region shear traction is proportional to the contact pressure ($|q(r)| = f|p(r)|$). Not constant pressure distribution, during time, could erroneously suggest that the slip length is different from the first half cycle in comparison to the next, however this is not possible otherwise at the end of each cycle a net advance of one portion of the contact would happen.

FE friction contact analysis was performed to solve contact pressure and shear traction distributions, indeed it was not possible to quantitatively transfer the external loading to local stress distribution through simple modeling. Since the fillet radius (2 mm) is very little in comparison to the tubular outside diameter (147 mm), plane strain condition is a good approximation, at the flat and rounded edge. Indeed local constraint is similar to the imposed plane strain condition, besides hoop stress, induced by radial interference, can be neglected in comparison to stresses concentration locally generated by the contact. The plane strain assumption will be explicitly exploited in the Finite Element (FE) model (more details are given later).

9

4 Fretting fatigue model selection

The flat and rounded contact has been widely investigated since it is a very common configuration where FF happens. Main recently developed approaches to characterize the FF are [15]:

(1) the asymptotic approach [22],
(2) multiaxial fatigue approaches [17,18,23].

4.1 Asymptotic approach

As previously introduced the flat and rounded geometry pressure distribution can be characterized by the *inner* asymptote (bounded) and the *outer* asymptote (singular). According to this approach, the generalized stress intensity factors K_I^* and K_{II}^* can be defined as the two parameters characterizing the *near edge* contact pressure and shear traction distributions: $p(r) = K_I^* \sqrt{r}$, $q(r) = 2/c \ K_{II}^* \sqrt{r}$, where r is the local coordinate starting from the edge of contact and c is the slip length. The two parameters completely measure the "strength" of the inner asymptote, either in terms of contact pressure and shear traction. The use of parameters $(K_I^*, \Delta K_{II}^*)$ is a very elegant way to fully characterize the fretting condition provided that slip length c is inside the round portion of contact. However, in the present paper fretting configuration, bulk stress cycles experiences large cyclic amplitude and the fillet radius is small, then the slip region is well extended inside the flat portion of the contact. Due to the large slip length inside the flat portion, the hot-spot is in the same condition with respect to the full sliding, in terms of stress distribution history. Indeed the stick/slip transition is far, then there is a portion of the cycle when the distribution of the shear traction equals the contact pressure distribution times the coefficient of friction, on a length which can be assumed larger than the fretting process zone at the hot spot, Fig. 6. The only difference with full sliding is that the slip per cycle is still of the order of microns (while in a full sliding configuration can be indefinitely larger). In this case of fretting the local solution (stress distribution history and slip history) can not completely characterized by parameters $K_I^*, \Delta K_{II}^*$ [22]. Therefore a generic multi-axial approach seems more promising.

4.2 Multiaxial fatigue approaches

An effective, and recent, example of multi-axial approach in FF is the work by Araújo and Nowell [17] proposing the use of the Fatemi–Socie (FS) critical plane approach. Only one stress parameter is considered, however the suggested averaging procedure allows for a correct interpretation of the size effect, particularly important in the FF problem where stress gradient is very high and the stress peak value would lead to very large underestimation of the fatigue strength.
A similar approach, recently proposed by Araújo et al. [18], is followed in the

present paper. Basically it is the application of the Theory of Critical Distance (TCD) [24,25], to the FF problem. The Point Method (PM) of the TCD provides a material related length L to properly take into account the size effect.

$$L = \frac{1}{\pi} \left(\frac{\Delta K_{th}}{\Delta \sigma_\infty} \right)^2 \tag{1}$$

where ΔK_{th} is the stress intensity factor threshold range and $\Delta \sigma_\infty$ is the plain specimen stress fatigue limit range, both obtained at fully reversed condition $R = -1$. Multiaxial stress state is taken into account through the use of the Modified Whöhler Curve Method (MWCM) [26] combined with the PM [27]. Following this approach, the stress state history is recorded at the depth of $L/2$ below the FF hot spot, Fig. 7.
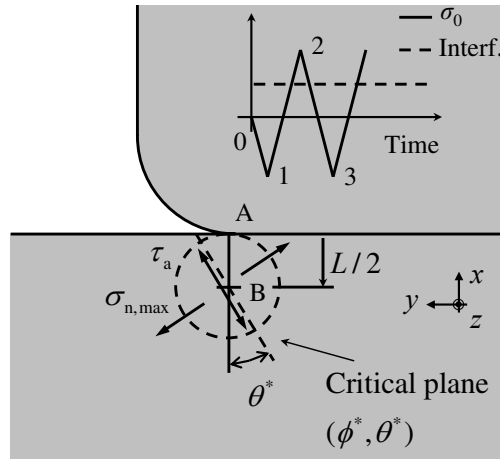

Fig. 7. Point method requires stresses evaluated at the position B, $L/2$ in depth from the hot spot, point A. Critical plane orientation is the one experiencing maximum shear amplitude during cyclic bending and it is defined by two angles ϕ^*, θ^*.

The equivalent shear stress amplitude (proposed by the MWCM) τ_a^{eq} is:

$$\tau_a^{eq} = \tau_a(\phi^*, \theta^*) + \left(\tau_\infty - \frac{\sigma_\infty}{2} \right) \rho(\phi^*, \theta^*) \tag{2}$$

where the angles ϕ, θ define a generic plane orientation and ϕ^*, θ^* define the plane experiencing the maximum shear amplitude τ_a, Fig. 7. The multi-axial load ratio ρ is defined as $\rho = \sigma_{n,max}/\tau_a$, where $\sigma_{n,max}$ is the maximum (during time history) normal stress acting on the ϕ^*, θ^* plane [26].

Material parameters τ_∞, σ_∞ are torsional and axial loading fatigue limits. Therefore the stress parameter τ_a^{eq} can be interpreted as a torsion equivalent shear stress, then the fatigue limit is defined by the condition:

$$\tau_a^{eq} \leq \tau_\infty \tag{3}$$

at the same probability as τ_∞ and σ_∞ are experimentally defined.

The MWCM is formulated also to predict the fatigue finite life other than the fatigue limit. Indeed it is possible to find the slope κ through a linear interpolation of (at least) two plain specimen S-N curve slopes, with different load ratios ρ: $\kappa_1 = \kappa(\rho_1)$

11

and $\kappa_2 = \kappa(\rho_2)$. More than two *S-N* curves could improve the accuracy, by fitting a linear trend between slope κ and load ratio ρ. It is also possible to calibrate parameters $(\tau_\infty - \sigma_\infty/2)$ and τ_∞ just applying the model at two plain specimen *S-N* curves.

As shown after, in the present paper, fatigue axial testing at $R = -1$ ($\rho_1 = 1$) and at $R = 0$ ($\rho_2 = 2$) were considered, only. Parameters τ_∞, σ_∞ and κ_1, κ_2 were found easily.

The use of the MWCM, combined with the PM, offers some advantages, for the application here proposed:

- experimental material parameters can be easily obtained from small specimen standard tests, for example the critical distance: L can be deduced just by processing results on notched specimens (as suggested in Ref. [28]), without the need of finding ΔK_{th} experimentally;
- friction contact analysis with linear elastic materials can be post-processed at least through FE analysis easily;
- fatigue life can be also considered through the MWCM.

4.3   Introduction of a slip parameter

It is well known that the fretting phenomenon can be classified as fretting *fatigue* and fretting *wear*, as shown in Fig. 8, after Vingsbo and Söderberg [29]. Sometimes the two fields of Fig. 8, are classified as partial slip (or mixed stick and slip) and gross (or full) slip (for example in Ref. [30]). However by classifying as partial vs. gross slip, the geometry is also involved (especially the fillet radius), while fretting fatigue vs. wear is more closely related to tribology.

The present configuration is partial slip. The slip amplitude is around 2-10 μm (results are shown later) therefore the condition of fretting fatigue is the case to be considered.
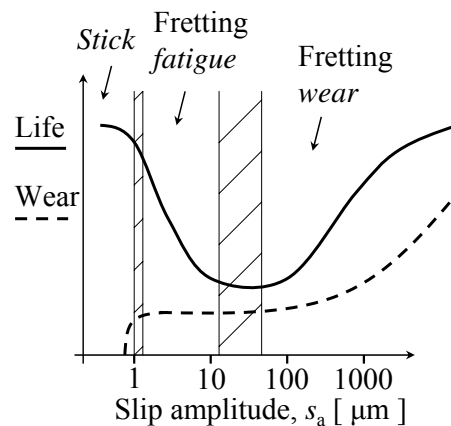

Fig. 8. Fretting *fatigue* distinguished from fretting *wear*. Low slip amplitude encourages the nucleation of cracks, while at higher slip, embryo cracks are etched due to the large amount of material removal.

The interpretation of Fig. 8 has been discussed extensively. Initially the high sensitive to slip amplitude suggested the use of slip parameters (or damage parameters) to fully capture the fretting fatigue, as the one defined by Ruiz (maximum shear traction times slip amplitude) [31]. Recently slip parameters are in disuse since they are considered empirical, indeed their physical basis is unclear [15,30]. More recently stress related approaches are preferred and the fretting fatigue slip sensitivity is considered to be simply a consequence of local higher shear stress which is in turn the actual reason of the fatigue crack nucleation. Anyway following this approach the fatigue life increase in the wear regime seems controversial. It is commonly accepted that in the wear regime 'embryo' cracks are removed before they can start to propagate, due to the large slip.

An important contribution about the present debate was recently introduced by Ding et al. [32] proposing the application of a FE wear model allowing for contact profile modification monitoring. Ding et al. were able to distinguish the partial slip regime to the gross slip regime, they noted that in both cases the contact profiles experience significant modification, but in the gross slip regime material removal is so large that contact is reduced to a more conforming contact configuration and this could be the explanation of the fatigue life increase in the wear regime. On the contrary stress severity is exacerbated in the partial slip regime, due to worse contact conformity after some wear non uniformly distributed, and this can be the explanation of fatigue life reduction in the fretting fatigue regime. Very recently Ding et al. [23] introduced a modified multiaxial SWT parameter including a correction which is function of the Ruiz parameter.

Similarly in the present paper it is suggested to admit a slip parameter to be considered in combination of the the TCD/MWCM stress parameter. Instead of formulating a combined fretting–multiaxial fatigue parameter, a bi–parameters map is simply proposed and a fatigue limit is delimited on this map, based on available experimental results. Deeper physical interpretation of the fretting fatigue phenomenon is not attempted in the present paper. The slip parameter here considered is simply the slip amplitude s_a at the end of contact $r = 0$ (Fig. 6) where the slip amplitude is maximum. Full scale test results are reported on the proposed bi–parameters map: stress parameter τ_a^{eq} and slip parameter s_a.

5   Results of the fretting model

5.1   *Determination of TCD/MWCM material parameters*

Drill pipes are produced through warm extrusion, therefore small specimens, to determine fatigue properties were easily obtained along the extrusion direction, while *compact test* specimens were difficult to be extracted since the thickness of the pipe is limited.

Therefore the critical distance L was available only through comparison between notched specimens, tested in axial loading at $R = -1$, and plain specimen tested in axial loading at $R = -1$. Stress distributions (FE simulation) along notch bisector

is shown in Fig. 9, the external load applied is equal to the fatigue limit for each notched geometry. The point where the stress distribution meet the plain specimen fatigue limit is half the critical distance L, according to the PM of the TCD.
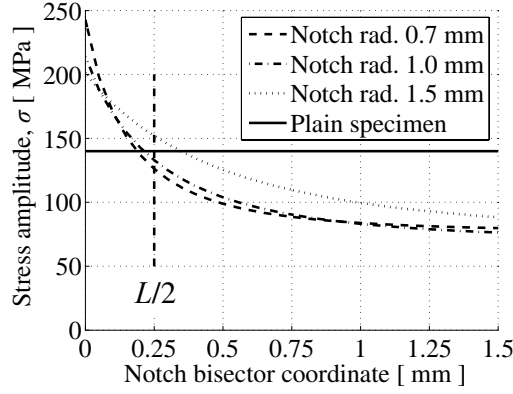

Fig. 9. Critical distance esteem through three notched specimen series.

It was found that the critical distance of the material is $L = 0.5$ mm. The scatter obtained is relatively small, Fig. 9.

The large value of L could seem surprising, but this aluminum alloy showed large amount of inclusions in its structure (as suggested by high contents of Fe and Si). Similarly to gray cast iron, the *internally flawed* structure leads to low fatigue limit, large fatigue scatter, but low notch sensitivity which can be translated in large critical distance [33].

Plain specimen axial loading at $R = -1$ resulted in $\sigma_\infty = 135$ MPa ($\Delta\sigma_\infty = 270$ MPa) considering the fatigue limit at $20\,10^6$, therefore the threshold stress intensity factor can be deduced: $\Delta K_{th} = 10.7$ MPa m$^{1/2}$ ($R = -1$).

MWCM parameters were obtained by means of two fatigue series, Fig. 10:

- plain specimen, axial loading, $R = -1$, $\rho_1 = 1$, obtaining $\sigma_{\infty,1} = \sigma_\infty = 135$ MPa, $\kappa_1 = 11.3$;
- plain specimen, axial loading, $R = 0$, $\rho_2 = 2$, obtaining $\sigma_{\infty,2} = 127$ MPa, $\kappa_2 = 41.2$.

The very high value of the κ_2 means that the *S-N* curve is almost flat, as shown in Fig. 10.

From these experimental results, according to the MWCM, it follows that $\tau_\infty = 71.5$ MPa (not very far from the von Mises criterion: $\tau_\infty \approx \sigma_\infty/\sqrt{3} = 77.9$ MPa).

For a generic loading condition the slope κ can be found as linear interpolation of the load ratio ρ:

$$\kappa(\rho) = \kappa_1 + \frac{\kappa_2 - \kappa_1}{\rho_2 - \rho_1}(\rho - \rho_1) \tag{4}$$

The slope κ is very sensitive to load ratio ρ for the material here considered, since κ_1 and κ_2 are quite dissimilar.
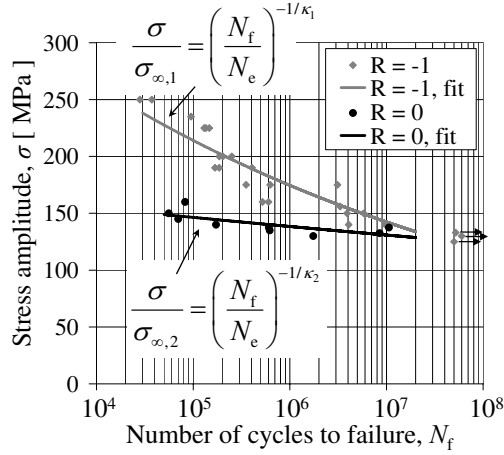
14

Fig. 10. Plain specimen testing at $R = -1$ and $R = 0$, very strong slope changing can be observed.

5.2 Finite element contact friction simulation

As already discussed, FE simulations were required to solve the contact problem, even though some features of the solution are available theoretically. To avoid cumbersome analysis, submodeling technique was applied. Then each load case was split into two simulation steps:

(1) the component loaded by radial interference and external bending σ_0 (with a 2D harmonic model);
(2) detailed local 2D plane strain submodel, loaded by displacements deduced from the global model previously solved.

The tubular connection is an axial-symmetry geometry (neglecting the thread helical angle, assuming thread as multiple rings). The radial interference could easily be modeled performing an axial symmetry analysis. To model tubular connection under bending it was possible to perform an analysis with axisymmetric harmonic elements [34]. Following this way a heavy 3D analysis was not required, Fig. 11 (a).

A local and finer submodel was created and displacements at the submodel boundaries obtained by interpolation from the global model solution previously obtained, Fig. 11 (b).

Loads P, Q and σ_b are not imposed directly, but they result after imposing the displacements at the boundaries of the submodel. More details about the use of the submodel technique in contact simulations with FE are provided in Ref.[35]. The submodel is performed under plane strain condition, assuming that it is a good approximation of the local stress state, as previously discussed. Displacements due to the interference were merged with displacements due to cyclic bending. The bending cycle was divided into 20 load steps.

The global model can feature closed gap instead of contact elements (keeping the analysis linear), tensile stress (instead of compressive) could appear if the contact would be opening, leading to bad contact simulation, but the present is not the case,
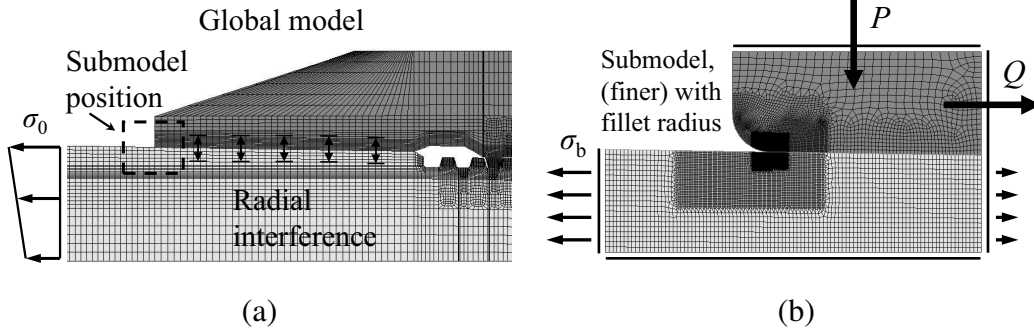
Fig. 11. (a) Portion of the global model. By modeling the component it is easy to impose radial interference and bending load σ_0. (b) Finer submodel, it is evident the degree of refinement required to properly simulate the high stress gradient at the contact hot spot.

since radial interference is enough to guarantee closed contacts everywhere. Contact friction analysis was performed on the finer submodel.

Coefficient of friction $f = 0.75$ was considered in the analysis since it is a typical value in fretting with aluminum alloys [1] (see for example Ref. [18]). Unfortunately coefficient of friction is reason of uncertainty of the procedure here shown and at the present state of research it was not possible to have a better esteem of it through laboratory experiment tests (for example as suggested in Ref. [19]). Motivation of this high value of f is that surface modification during fretting can lead to friction increase [36], however the effective coefficient of friction is strongly related to materials in contact and to the level of slip, while it is not very sensitive to the initial state of the surface before fretting.

5.3 Stress parameter results

The point method requires the calculation of the stresses history at $L/2$ depth, point B of Fig. 7. The orientation of the critical plane is perpendicular the plane of the problem for symmetry reason, then only one angle θ^* is required to define the critical plane. In Fig. 12 (a) the time history of stresses at position B are reported, for a bending loading $\sigma_0 = 50$ MPa, at the Box side of the connection (chamfer angle $18°$, Fig. 4).

Stress components are slightly not proportional at this depth, Fig. 12 (a). Stresses τ_a and $\sigma_{n,max}$ are shown in Fig. 12 (b) as function of θ coordinate.

Obviously the period of function $\tau_a(\theta)$ is $\pi/2$, while the period of function $\sigma_{n,max}(\theta)$ is π, then there are two orientations where τ_a is maximum, the one experiencing higher $\sigma_{n,max}$ is the critical plane. For the present load $\theta^* = 32.4°$ at $L/2$ depth from the hot spot.

To have an idea of the (multiaxial) stress gradient near the hot spot, Fig. 13 shows stresses time history and polar function of τ_a and $\sigma_{n,max}$ at the hot spot, point A of Fig. 7.

---

[1] Obviously the coefficient of friction depends on the material combination, $f = 0.75$ is a typical value for aluminum in contact with aluminum. Reliable data for fretting coefficient of friction between steel and aluminum was not found in literature by the author.
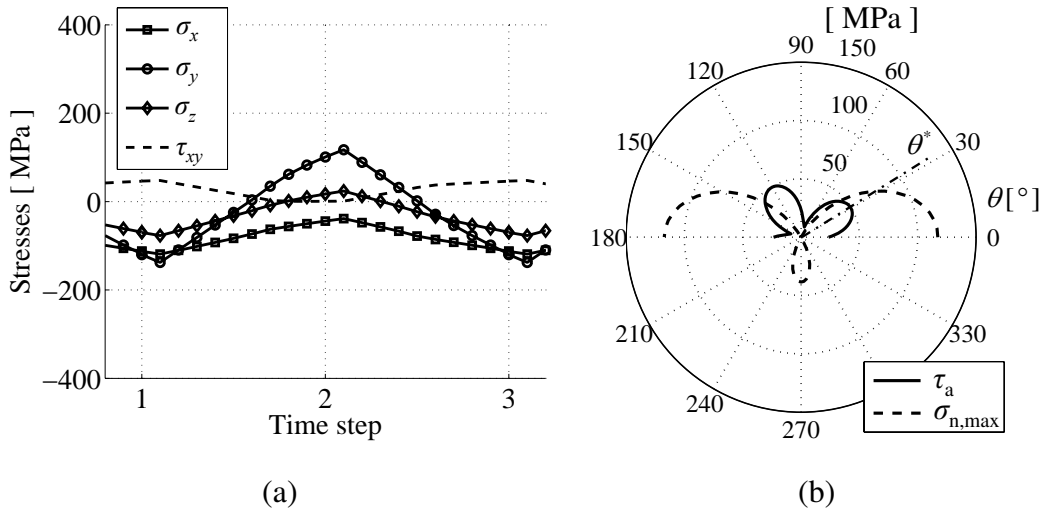
Fig. 12. (a) Stresses time history at $L/2$ below the hot spot (point B). (b) Polar presentation of τ_a and $\sigma_{n,max}$ at $L/2$ below the hot spot (point B). The critical plane is defined by the angle θ^* experiencing maximum τ_a.
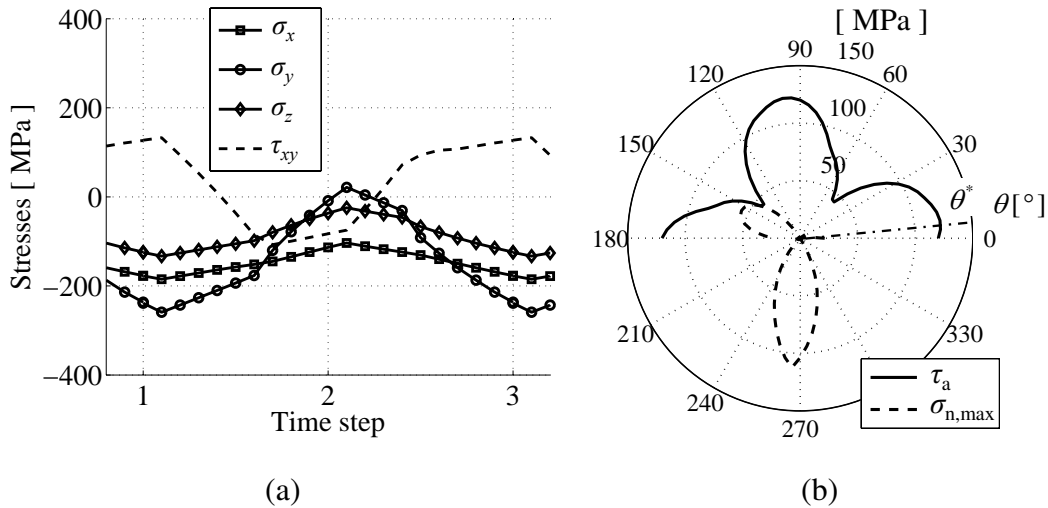

Fig. 13. (a) Stresses time history at the hot spot. (b) Polar presentation of τ_a and $\sigma_{n,max}$ at the hot spot. The critical plane is defined by the angle θ^* experiencing maximum τ_a.

It is possible to see that stress τ_a changes steeply from point A to B, and $\sigma_{n,max}$ is fully compressive at point A, while it is tensile at point B. Critical plane orientation change very much, from almost vertical to more than $30°$.

By computing von Mises equivalent stress, at the hot spot point A, during stress time history of Fig. 13 (a), it follows that the equivalent stress is always lower than the yield strength, during bending (at $\sigma_0 = 50$ MPa), at least accordingly to solid elastic mechanics, even though a large coefficient of friction $f = 0.75$ was considered in the model.

5.4 Slip parameter results

As discussed before the slip amplitude is considered along with the multiaxial stress.

Fig. 14 (a) shows the slip distribution s along the contact (coordinate r) defined as the difference between the relative position at a generic time and the relative position when the radial interference is applied before bending. Slip at the position $r = 0$ (termed as s_0) is shown in Fig. 14 (b), along with maximum pressure fluctuation during time. Time steps used in Fig. 14 are defined in Fig. 7. The slip amplitude s_a is half the range of s_0 during time.
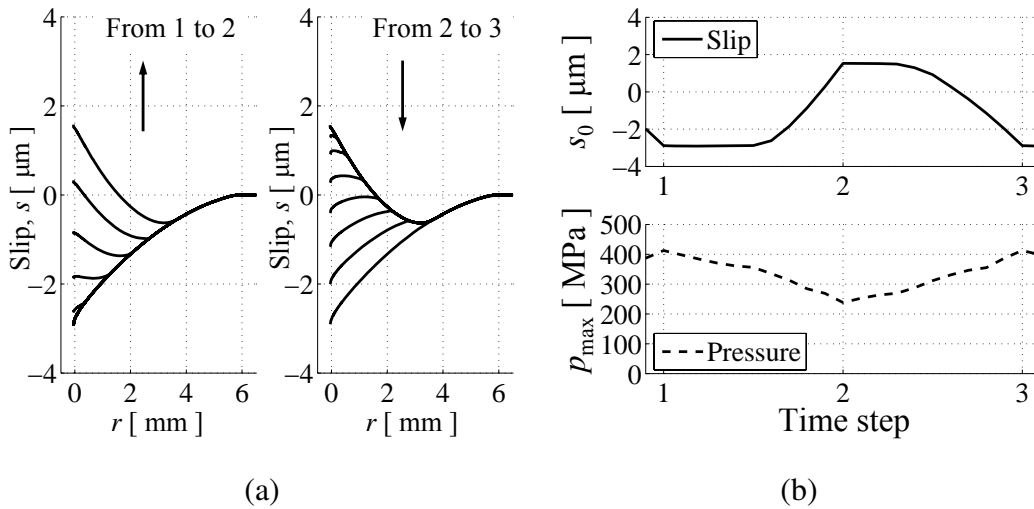

Fig. 14. (a) Slip distribution along contact coordinate r, during time steps. (b) Slip s_0 and maximum pressure p_{max}, during time steps.

The slip length due to the first application of bending, from time 0, when radial interference is applied before bending, to time 1 when bending experiences its first reversal, is about 6.0 mm (for the present load) and it is somewhat different to the cyclic slip length c which is less than 4.0 mm, Fig. 14 (a). From Fig. 14 (b) it is clear how the pressure changes significantly during the cycle. Due to the contact pressure changing it follows that the slip trend from time 1 to 2 is not just reversed as compared to slip from time 2 to 3. Indeed in the first half of the cycle (from time 1 to 2) the more compression, after the reversal, generates slip start retardation in comparison to the next half (from time 2 to 3).

5.5 Interpretation of full scale test results

Parameters τ_a^{eq} and s_a found for each full scale test, Fig. 15. As shown in Fig. 4, two critical locations are present at the two connection sides. These two locations are here referred as Pin and Box, the only difference is the chamfer angle which is smaller for the Box side, Fig. 4. It is evident that the stress parameter is slightly higher for the Pin side as compared to the Box which features a less severe chamfer. Opposite trend can be observed about the slip amplitude.
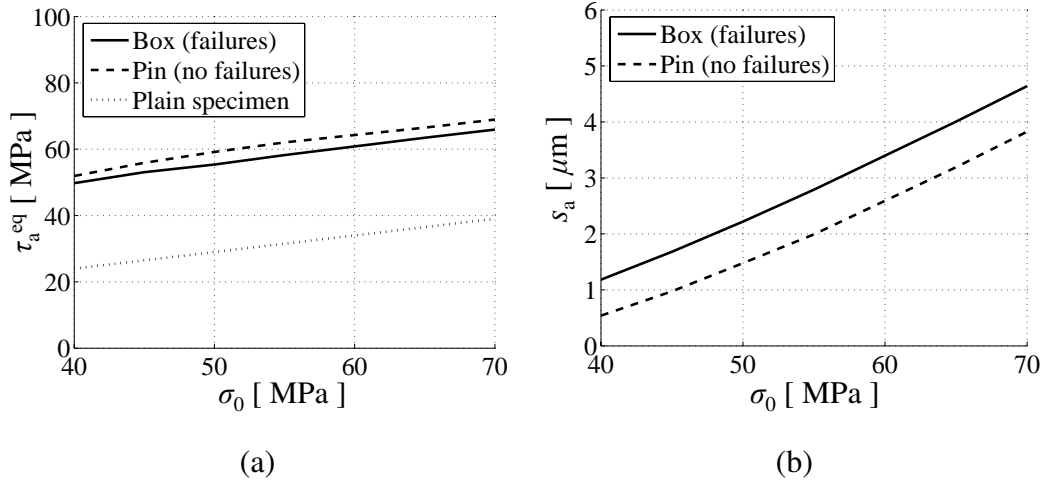
18

Fig. 15. (a) Stress parameter τ_a^{eq} at the two sides of the connection. (b) Slip amplitude s_a at the two sides of the connection.

From the knowledge of τ_a and ρ, at the PM location, the MWCM produced the fatigue life prediction, reported in Fig. 16.
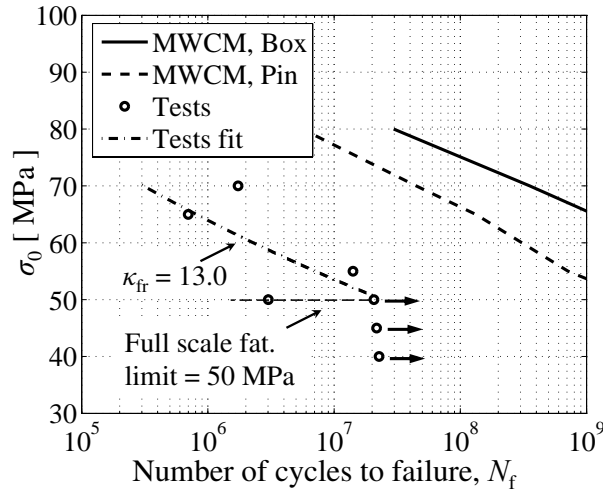

Fig. 16. Fretting fatigue finite life, test results vs. TCD/MWCM model.

About results of Fig. 16 some remarks are needed:

- since the stress level is higher for the Pin side, Fig. 15 (a), the fatigue life predicted is lower, but opposite trend was observed from experiment tests, since failures were obtained at the Box side only;
- the lower stress is compensated by the higher slip (according to the thesis of the present paper), which is higher for the Box side, Fig. 15 (b);
- therefore the TCD/MWCM itself leads to a counter conservative esteem of the fatigue life, since slip plays a further damaging role which the multiaxial criterion is insensitive to.

The bi–parameters map (stress–slip) is reported in Fig. 17. All full scale tests are reported on the map according to their τ_a^{eq} and s_a coordinates.
A 'generalized fatigue limit' (at $20\,10^6$ cycles) is eventually deduced by imposing
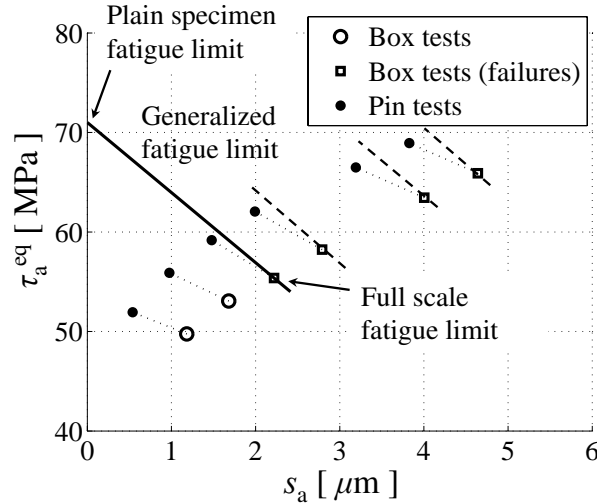
19

Fig. 17. Stress–slip map. The generalized fatigue limit is deduced, from the knowledge of the plain specimen fatigue limit (no slip) and the full scale fatigue limit.

two conditions:

(1) the fatigue limit of the plain specimen at the condition of no slip, i.e. at $s_a = 0.0$ μm coordinate of the map;
(2) the full scale tests fatigue limit, corresponding to the Box side loaded at $\sigma_0 = 50$ MPa.

A linear limit was simply drawn between these two points, however there is no reason for the generalized fatigue limit to be exactly linear, anyway it is the simplest choice if only two points are known. Both points are defined at (50% of probability), in particular for the Box side loaded at $\sigma_0 = 50$ MPa only two tests were available (one failure, one run out). Unfurtately producing many tests on the present components was too demanding. A clear result of Fig. 17 is that the Pin side (experiencing no failure) appears in safer condition with respect to the Box side (experiencing all failures), either at the fatigue limit and for higher loads too, as emphasized by the dashed lines of Fig. 17, assuming same slope in the finite life regime.

6 Discussion

The use of TCD/MWCM stress amplitude parameter τ_a^{eq} along with the slip parameter s_a offers a good correlating tool to rationalize fretting fatigue tests, for partial slip condition. Indeed it was possible to identify the worse between two similar configurations Fig.17 (even though with little margin) in agreement with experimental evidence of full scale tests.
It is remarkable that in the case of small slip the TCD/MWCM showed good results without the need of a further slip related parameter, as well documented in Ref. [18], then the present paper offers an extension of this model for larger slip. For the fretting case, where slip is confined in the round portion of the contact,

20

the use of K_I^* and ΔK_{II}^* is already a satisfactory tool to characterize fretting, since a slip related parameter is intrinsically embedded in ΔK_{II}^*. Indeed it is possible to decouple them in ΔK_{II}^* and c, that can be interpreted as a stress parameter and a slip parameter. The parameter proposed by Ding et al. [23] offers many similarities, indeed the multiaxial SWT parameter was used and a correction provided according to fretting Ruiz parameter, but no consideration was provided to take into account the size effect, since the peak value was simply considered.

Obviously the use of the here defined map requires standard material fatigue tests but fretting tests too. An advice is to take tests with slip amplitude near to that of the actual components, since the linear extrapolation may not be reliable if tests to calibrate the map and actual components conditions are quite dissimilar.

The use of the term 'fatigue limit' in the present paper is questionable, and should be replaced with 'fatigue endurance' up to a certain number of cycles ($N_e = 20 \, 10^6$ for the present application). Indeed the arrest of the fretting phenomenon was not investigated, moreover aluminum alloys are typical examples of materials that do not show a clear fatigue limit.

The little accuracy about the knowledge of the coefficient of friction is not so restrictive, if the present map is considered. Indeed the here suggested use of phenomenological correlating parameters, compensate (at least partly) the ignorance of it. For example imposing lower f in the model than the actual value, produces lower shear stress *but* it also produces higher slip, and vice versa imposing higher f. Thus fretting tests, once reported on the stress–slip map, have a scatter (due to friction coefficient uncertainty) that follows the trend of the generalized fatigue limit (higher slip, lower stress) then its definition appears more robust.

More investigation is still required particularly about the consistency of the slip parameter s_a in terms of capturing the fretting configuration in conjunction with TCD/MWCM τ_a^{eq} parameter. Furthermore the generalized fatigue limit is not necessarily linear, especially for large slip where the transition from fretting fatigue to fretting wear has opposite trend with respect to that in the fretting fatigue regime.

7 Conclusions

(1) A stress–slip map is here proposed to interpret fretting fatigue full scale tests on aluminum drill pipe to steel connections.

(2) Two different configurations were compared, and the map was able to identify the worse in agreement with experimental evidence.

(3) By dedicated tests, for a given combination of materials, it is also possible to produce the map, avoiding expensive (and time consuming) full scale tests.

(4) The scope of the present fretting correlating parameters is the partial slip condition with slip extended in the flat portion of contact, in this case the slip amplitude is not completely embedded in the stress parameter.

(5) Process volume under multiaxial fatigue, assisted by surface fretting damaging, is the physical basis behind the definition of the two parameters for the map.

(6) The use of the present map is an effective tool for evaluating proposals of

design modifications to improve fatigue performance of the connection, for example the role of grooves, on the aluminum cylindrical surface, near the hot spot, or modification of the steel wall thickness, or modification of the aluminum pipe wall thickness.

(7) Standard fatigue material data are needed, along with fretting test results, to distinguish the surface damaging role of slip.

(8) Cumbersome friction contact simulations can be limited to a small portion of the model, through the submodeling technique. Already existing models of the whole structure can be exploited as global models for the first simulation step, after it is possible to interpolate displacements to be used as submodel input.

(9) Obviously more data would be required to better define the generalized fatigue limit. To pursue this task, small scale fretting tests can be performed avoiding demanding full scale tests.

Acknowledgments

References

[1] H. Rabia. *Oil Well Drilling Engineering: principles and practice*. Graham and Trotman, 1985.

[2] O. Vaisberg, O. Vincké, G. Perrin, J. P. Sarda, and J. B. Faÿ. Fatigue of drillstring: State of art. *Oil and Gas Science and Technoogy*, 57(1):7–37, 2002.

[3] A. Baryshnikov, A. Calderoni, A. Ligrone, and P. Ferrara. A New Approach to the Analysis of Drillstring Fatigue Behavior. *SPE Drilling and Completion*, 12(2):77–84, 1997.

[4] P. D. Spanos, A. M. Chevallier, and N. P. Politis. Oil well drilling: A vibrations perspective. Technical report, Rice University, 2001. Preprints of the Department of Mechanical Engineering and Material Science.

[5] M. Ya, V.S. Basovich, and V.S. Tikhonov. Drillstring with aluminum alloy pipes design and practices. Society of Petroleum Enginners, 2003. n° 79873.

[6] ISO 15546. Petroleum and natural gas industries – Aluminium alloy drill pipe, 2002. 1st edition.

[7] American Society for Metals. ASM handbook. In ASM International, editor, *Properties and selection: nonferrous alloys and special–purpose materials*, volume 02. Metals Park, OH: American Society for Metals, 1990.

[8] L. Bertini, M. Beghini, C. Santus, and A. Baryshnikov. Resonant test rigs for fatigue full scale testing of oil drill string connections. *International Journal of Fatigue*, 2007. Submitted for pubblication.

[9] S. Faanes. Inclined cracks in fretting fatigue. *Engineering Fracture Mechanics*, 52(1):71–82, 1995.

[10] R.B. Waterhouse. *Fretting Fatigue*. Applied Science Publishers Ltd - London, 1981.

[11] C. Churchman, A. Mugadu, and D. A. Hills. Asymptotic results for slipping complete frictional contacts. *European Journal of Mechanics A/Solids*, 22(6):793–800, 2003.

[12] J. Dundurs and M.S. Lee. Stress concentration at a sharp edge in contact problems. *Journal of Elasticity*, 2(2):109, 1972.

[13] A.E. Giannakopoulos, T.C. Lindley, and S. Suresh. Aspect of equivalence between contact mechanics and fracture mechanics: theoretical connections and a life-prediction methodology for fretting-fatigue. *Acta Materialia*, 46(9):2955–2968, 1998.

[14] K.L. Johnson. *Contact Mechanics*. Cambridge University Press, 1985.

[15] D. Nowell, D. Dini, and D.A. Hills. Recent developments in the understanding of fretting fatigue. *Engineering Fracture Mechanics*, 73:207–222, 2006.

[16] D. A. Hills and D. Dini. A new method for the quantification of nucleation of fretting fatigue cracks using asymptotic contact solutions. *Tribology International*, 39:1114–1122, 2006.

[17] J.A. Araujo and D. Nowell. The effect of rapidly varying contact stress fields on fretting fatigue. *International Journal of Fatigue*, 24:763 – 775., 2002.

[18] J.A. Araújo, L. Susmel, D. Taylor, J.C.T. Ferro, and E.N. Mamiya. On the use of the Theory of Critical Distances and the Modified Wöhler Curve Method to estimate fretting fatigue strength of cylindrical contacts. *International Journal of Fatigue*, 29:95–107, 2007.

[19] D.A. Hills and D. Nowell. *Mechanics of Fretting Fatigue*. Kluwer accademic publishers, 1994.

[20] A. Mugadu, D.A. Hills, J.R. Barber, and A. Sackfield. The application of asymptotic solutions to characterising the process zone in almost complete frictional contacts. *International Journal of Solids and Structures*, 41:385–397, 2004.

[21] M. Beghini and C. Santus. Analysis of the plane contact with discontinuous curvature. *MECCANICA*, 42:95–106, 2007.

[22] D. Dini and D. A. Hills. Bounded asymptotic solutions for incomplete contacts in partial slip. *International Journal of Solids and Structures*, 41:7049–7062, 2004.

[23] J. Ding, W.S. Sum, R. Sabesan, S.B. Leen, I.R. McColl, and E.J. Williams. Fretting fatigue predictions in a complex coupling. *International Journal of Fatigue*, 29:1229–1244, 2007.

[24] D. Taylor. Geometrical effects in fatigue: a unifying theoretical model. *International Journal of Fatigue*, 21:413–420, 1999.

[25] D. Taylor and G. Wang. The validation of some methods of notch fatigue analysis. *Fatigue & Fracture of Engineering Materials and Structures*, 23:387–394, 2000.

[26] L. Susmel and P. Lazzarin. A bi-parametric Wöhler curve for high cycle multiaxial fatigue assessment. *Fatigue & Fracture of Engineering Materials and Structures*, 25:63–78, 2002.

[27] L. Susmel. A unifying approach to estimate the high-cycle fatigue strength of notched components subjected to both uniaxial and multiaxial cyclic loadings. *Fatigue & Fracture of Engineering Materials and Structures*, 27:391–411, 2004.

[28] D. Taylor, P. Bologna, and K. Bel Knani. Prediction of fatigue failure location on a component using a critical distance method. *International Journal of Fatigue*, 22:735–742, 2000.

[29] O. Vingsbo and S. Söderberg . On fretting maps. *Wear*, 126:131–147, 1988.

[30] T.C. Lindley. Fretting fatigue in engineering alloys. *International Journal of Fatigue*, 19:S39–S49, 1997.

[31] C. Ruiz, P.H.B. Boddington, and K.C. Chen. Investigation of fatigue and fretting in a dovetail joint. *Experimental Mechanics*, 24(3):208–217, 1984.

[32] J. Ding, S.B. Leen, and I.R. McColl. The effect of slip regime on fretting wear–induced stress evolution. *International Journal of Fatigue*, 26:521–531, 2004.

[33] D. Taylor. Analysis of fatigue failures in components using the theory of critical distances. *Engineering Failure Analysis*, 12(6):906–914, 2005.

[34] ANSYS Inc. *User's manual, version 10.0.* 201 Johnson Road, Houston (PA, 15342–1300), 2005.

[35] R. Rajasekaran and D. Nowell. On the finite element analysis of contacting bodies using submodelling. *The Journal of Strain Analysis for Engineering Design*, 40(2):95–106, 2005.

[36] D.R. Swalla and R.W. Neu. Influence of coefficient of friction on fretting fatigue crack nucleation prediction. *Tribology International*, 34:493–503, 2001.
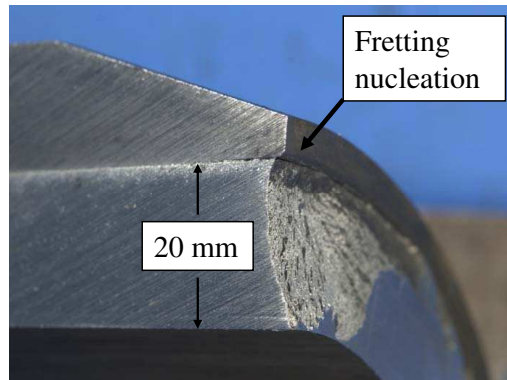
A Color figures for online version of the paper

Fig. A.1. Color version of Fig. 5 (a).